Production and evaluation of silicon immersion gratings for infrared astronomy

J. P. Marsh, D. J. Mar, and D. T. Jaffe*

Department of Astronomy, University of Texas at Austin, Austin, Texas 78712, USA

*Corresponding author: dtj@astro.as.utexas.edu

Received 18 October 2006; revised 30 January 2007; accepted 31 January 2007;
posted 5 February 2007 (Doc. ID 76195); published 18 May 2007

Immersion gratings, diffraction gratings where the incident radiation strikes the grooves while immersed in a dielectric medium, offer significant compactness and performance advantages over front-surface gratings. These advantages become particularly large for high-resolution spectroscopy in the near-IR. The production and evaluation of immersion gratings produced by fabricating grooves in silicon substrates using photolithographic patterning and anisotropic etching is described. The gratings produced under this program accommodate beams up to 25 mm in diameter (grating areas to 55 mm × 75 mm). Several devices are complete with appropriate reflective and antireflection coatings. All gratings were tested as front-surface devices as well as immersed gratings. The results of the testing show that the echelles behave according to the predictions of the scalar efficiency model and that tests done on front surfaces are in good agreement with tests done in immersion. The relative efficiencies range from 59% to 75% at 632.8 nm. Tests of fully completed devices in immersion show that the gratings have reached the level where they compete with and, in some cases, exceed the performance of commercially available conventional diffraction gratings (relative efficiencies up to 71%). Several diffraction gratings on silicon substrates up to 75 mm in diameter having been produced, the current state of the silicon grating technology is evaluated. © 2007 Optical Society of America

OCIS codes: 050.1950, 300.6340, 350.1260.

1. Introduction

The silicon grating group at the University of Texas has spent the last 15 years developing techniques for etching precisely placed grooves into monocrystalline silicon substrates, as well as shaping and coating these substrates in order to produce silicon grisms [1,2] and echelle gratings [1,3–6]. The goal of our silicon echelle program is to produce gratings that can be used as immersion echelles from 1.1 to 5 μm. These devices permit compact optical designs of high-resolution near-IR spectrographs.

A. Principles of Operation

An immersion grating is a ruled diffraction grating in which the light strikes grooves from inside a medium with index of refraction, n, greater than 1. Upon being diffracted, light exits either through the same entrance face or an appropriately positioned exit face.

The main advantage of immersion gratings over front-surface devices is that of resolving power versus grating length and therefore the overall mass and volume of the grating spectrometer. The maximum attainable resolving power $R = \lambda/\Delta\lambda$ for a grating immersed in a medium with refractive index n, when used in a Littrow configuration is given by

$$R = \frac{2nL \sin \delta}{\lambda} = \frac{2nW \tan \delta}{\lambda} = mN, \quad (1)$$

where L is the illuminated length of the grating, W is the beam diameter, δ is the blaze angle, λ is the vacuum wavelength, N is the number of illuminated grooves, and m is the diffraction order. The difference between a front-surface grating and an immersion grating of the same size arises because the wavelength of light in a dielectric is decreased by a factor of n. This decrease makes the phase difference between the extremes of the illuminated parts of the grating surface n times larger (Fig. 1) and increases

0003-6935/07/173400-17$15.00/0
© 2007 Optical Society of America

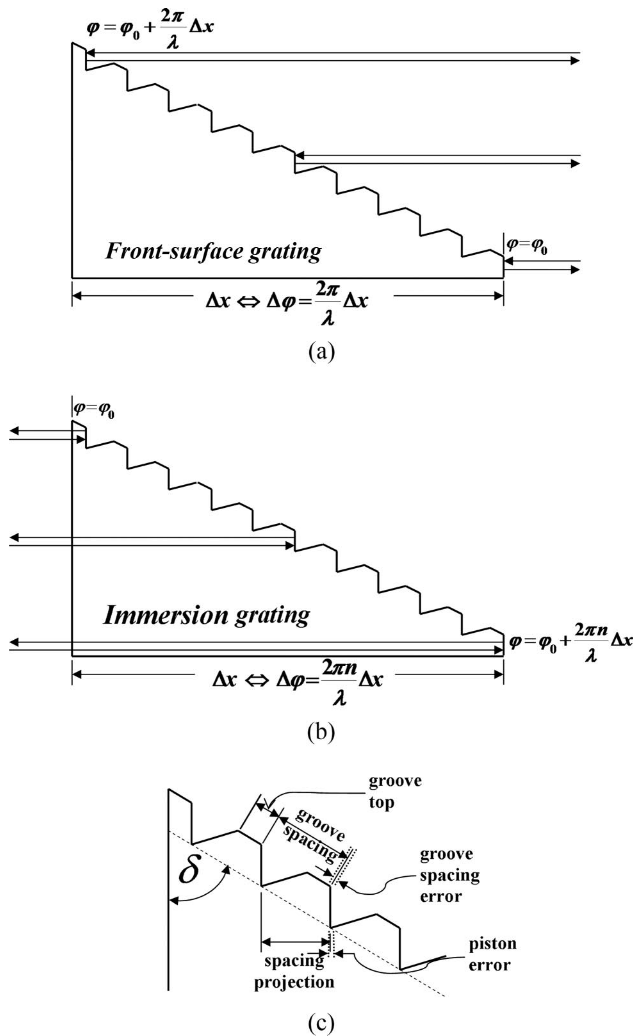

Fig. 1. Schematic of an etched silicon grating used in different modes: (top) front-surface grating with light incident from the right; (middle) immersion grating with light incident from the left. The phase difference between the first and the last groove is n times larger when the light passes through a medium with index of refraction n. The bottom panel shows an enlarged view of the ruled surface. The ruled grooves are separated by flat groove tops that served as etch stops during the manufacturing process. The groove spacing and allowable spacing error are related to the projected spacing and the groove piston error through the blaze angle δ (see text).

the resolving power by the same factor. The grating equation inside the medium is

$$m\lambda = \sigma n(\sin \alpha' + \sin \beta'), \quad (2)$$

where σ is the groove period, and α′ and β′ are the incident and diffracted angles inside the material. Equation (2) implies that the immersed echelle operates in an order which is n times the order of a non-immersed echelle. In addition to the increased resolving power, immersion gratings have a larger angular dispersion. The angular dispersion outside the immersing medium, $d\beta/d\lambda$, is given by

$$\frac{d\beta}{d\lambda} = \frac{m}{\sigma \cos \delta} = \frac{\sin \alpha + \sin \beta}{\lambda \cos \beta}, \quad (3)$$

where α and β are the incident and diffracted angles outside the material. There is an $n$fold increase in the angular dispersion, which one can think of as resulting either from the increase in the diffraction order by a factor of n, or as a result of Snell's law and the refraction of light at the material–air interface.

In IR astronomy and in atmospheric science, it is often helpful to be able to cover large continuous wavelength regions in single exposures at high resolving power. At optical wavelengths, cross-dispersed echelle spectrometers with large-format CCD detectors routinely cover bands of $\Delta\lambda/\lambda = 0.2$ at resolving powers of 40,000 or more [7–9]. In the IR, there are as yet no high resolution instruments at comparable resolving power with continuous wavelength coverage larger than $\Delta\lambda/\lambda = 0.014$ [10]. The difference stems from the limited size of current IR detector arrays and, more importantly, from the limitations on the maximum groove spacing available in ruled gratings (~50 μm). While gratings with larger groove spacings do exist [11,12], they are neither readily available nor precise enough for high diffraction efficiency in the near-IR. With micromachined immersion gratings, the increase in the order number by a factor of n, coupled with an ability to produce coarse grooves, makes possible the design of cross-dispersed echelle spectrographs with continuous spectral coverage over large ranges in wavelength. The number of diffraction-limited spectral resolution elements per order equals the number of illuminated grooves, N. Since the resolving power R of a grating equals the product of the order number m and the number of illuminated grooves N, higher resolving power at a fixed order number leads to larger numbers of resolution elements per order. In the IR, where detector array sizes are limited, it is hard to sample an entire order adequately unless the grating is of very high order. This result makes immersion echelles a perfect choice for compact, cross-dispersed spectrographs covering large stretches of continuous wavelength space.

B. History

The principle of immersion gratings was first described by Fraunhofer who experimentally determined the grating equation for diffractive optics immersed in various fluids [13,14]. It was rediscovered half a century ago [15]. An immersion grating concept based on ion milling of germanium was patented in 1984 [16] but was never put into practice. Work on immersion gratings started appearing in the astronomical literature in the late 1980s. Early investigations used diffraction gratings immersed in BK7 glass [17] and quartz [18], with additional work continuing in recent years [19,20]. In the IR, several groups began to experiment with diffraction gratings chemically etched in silicon [3,21–27]. Other groups have produced prototype immersion gratings by diamond-machining grooves in various materials [28], including germanium [29,30], ZnS, ZnSe [31,32], and thallium bromoiodide [33].

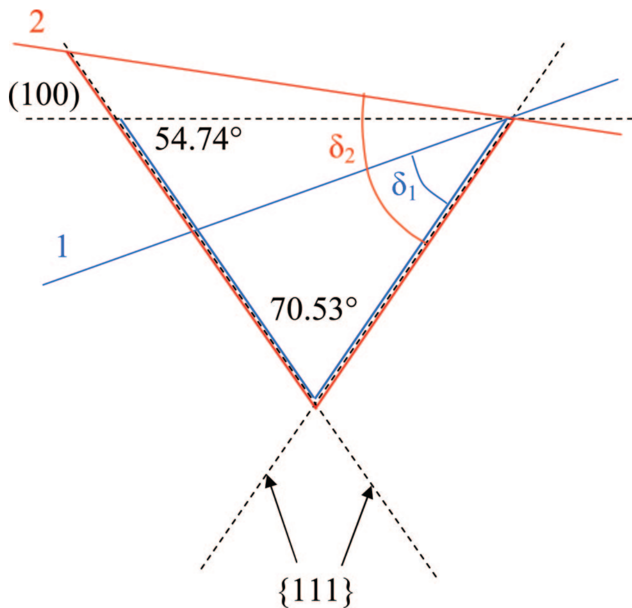

Fig. 2. (Color online) Relationship between silicon crystal planes and blaze angle. The positions of the (111) and (100) planes are indicated by dashed lines. Cutting a surface in the silicon boule at the (100) plane results in a blaze at the natural angle of 54.74°. Cuts 1 and 2 will result in blaze angles δ_1 (<54.74°) and δ_2 (>54.74°), respectively.

C. Silicon Properties

The choice of silicon for IR immersion gratings is advantageous both because of its high index of refraction ($n = 3.44$ at 2.5 μm, $T = 295$ K) and because of a vast technological knowledge base supported by decades of development by the silicon semiconductor industry for electronics applications. Silicon is available in boule diameters up to 30 cm and in a range of resistivities, from a few Ω cm in highly doped material to a few thousand Ω cm in the highest purity undoped material. The material properties of silicon are well suited to the needs of IR spectroscopy [34]. Its low coefficient of thermal expansion (ranging between -0.5×10^{-6} K^{-1} at 77 K and 2.6×10^{-6} K^{-1} at 300 K) [35,36] translates into small changes in the blaze wavelength when the grating is cooled, and its high thermal conductivity (between 1300 W m^{-1} K^{-1} at 77 K and 160 W m^{-1} K^{-1} at 300 K) [37] results in short cool-down times for silicon optics in cryogenic systems. Crystalline silicon has a very small coefficient of absorption from ~1.2 to ~6.5 μm [38–40]. The short wavelength cutoff shifts to shorter wavelengths at lower temperatures [41].

Much silicon processing takes advantage of the crystal plane geometry of monocrystalline silicon and of anisotropic etchants such as aqueous potassium hydroxide (KOH), which etches silicon {100} planes much faster than {111} planes [42]. If we cut a silicon wafer so that a (100) plane is exposed and, along the intersections of {100} and {111} planes, place a series of stripes in a material resistant to etching by KOH, the high anisotropy ratio (the ratio of the etch rates across the crystal planes) of the solution for the {100} and {111} planes results in symmetric, V-shaped grooves with their walls defined by slow etching {111} planes [43]. The intersecting {111} planes define a groove opening angle of 70.53° instead of the 90° angle common to most ruled gratings. The resulting grating is blazed at 54.74°. To produce a grating with a blaze angle different than 54.74°, we expose a surface that has been rotated with respect to the (100) plane (Fig. 2). The etchant exposes (111) planes in this case as well, but the resulting profile is asymmetric and blazed at the desired angle δ.

In addition to having different opening angles, micromachined gratings have a flat groove top, which occurs as a result of the manufacturing process (Fig. 1). For high-order gratings used in immersion, the smaller valley angle and the groove tops should have no effect since the vertices and the tops are hidden behind groove walls. When used in high orders, gratings operate in the scalar limit, and the performance of an error-free silicon immersion grating is indistinguishable from that of an error-free ruled reflection grating operating in the same order. However, in low orders, a more rigorous approach using vector modeling should be used because the wavelengths at which the grating operates are comparable to the groove width, and the grooves are no longer simple reflecting surfaces [44]. Our group has investigated the behavior of low-order gratings theoretically [45], and found that, even in low order, the measured efficiencies of micromachined silicon gratings are very close to those of comparable ruled gratings [3].

We outline here the production and analysis of three immersion gratings, G0, G1, and G3. The physical parameters of these gratings are listed in Table 1. G1, completely cut and equipped with antireflection and metallized coatings, was designed for use in a spectrograph proposed for the NASA Infrared Telescope Facility (IRTF). G0, also completely cut and coated, was a prototype used to test many concepts that were subsequently applied to G1. G1's successor G3 is a completed grating, cut but not yet coated. We will talk about the process of

Table 1. Immersion Grating Physical Design Parameters

Grating	Blaze Angle δ	Groove Spacing σ	Groove Top τ	Passivation Material and Thickness	Mask
G0	54.7°	142 μm	10 μm	600 nm thermal oxide	Ruled
G1	63.4°	80 μm	6 μm	60 nm silicon nitride	Photolithographic
G3	32.6°	87 μm	6 μm	60 nm silicon nitride	Photolithographic

chemically ruling grooves into silicon crystal as well as the tolerances for this process, show results from tests performed on our gratings and the analysis of grating errors and their sources, and summarize the results of our research to date.

2. Material Processing

There are three stages in the production of silicon immersion gratings, as illustrated in Fig. 3: substrate preparation (steps 1–5, which include growing the boule, orientation, cutting, polishing, and coating with a passivation layer and a photoemulsion), production of the grooves (steps 6–11, which includes transferring a pattern of stripes from a mask to the passivation layer and chemical ruling using anisotropic etching), and shaping and coating the substrate of the grating for use in immersion (steps 12–13). We discuss here the tolerances required to produce useful devices and then go through the details of the process outlined in Fig. 3.

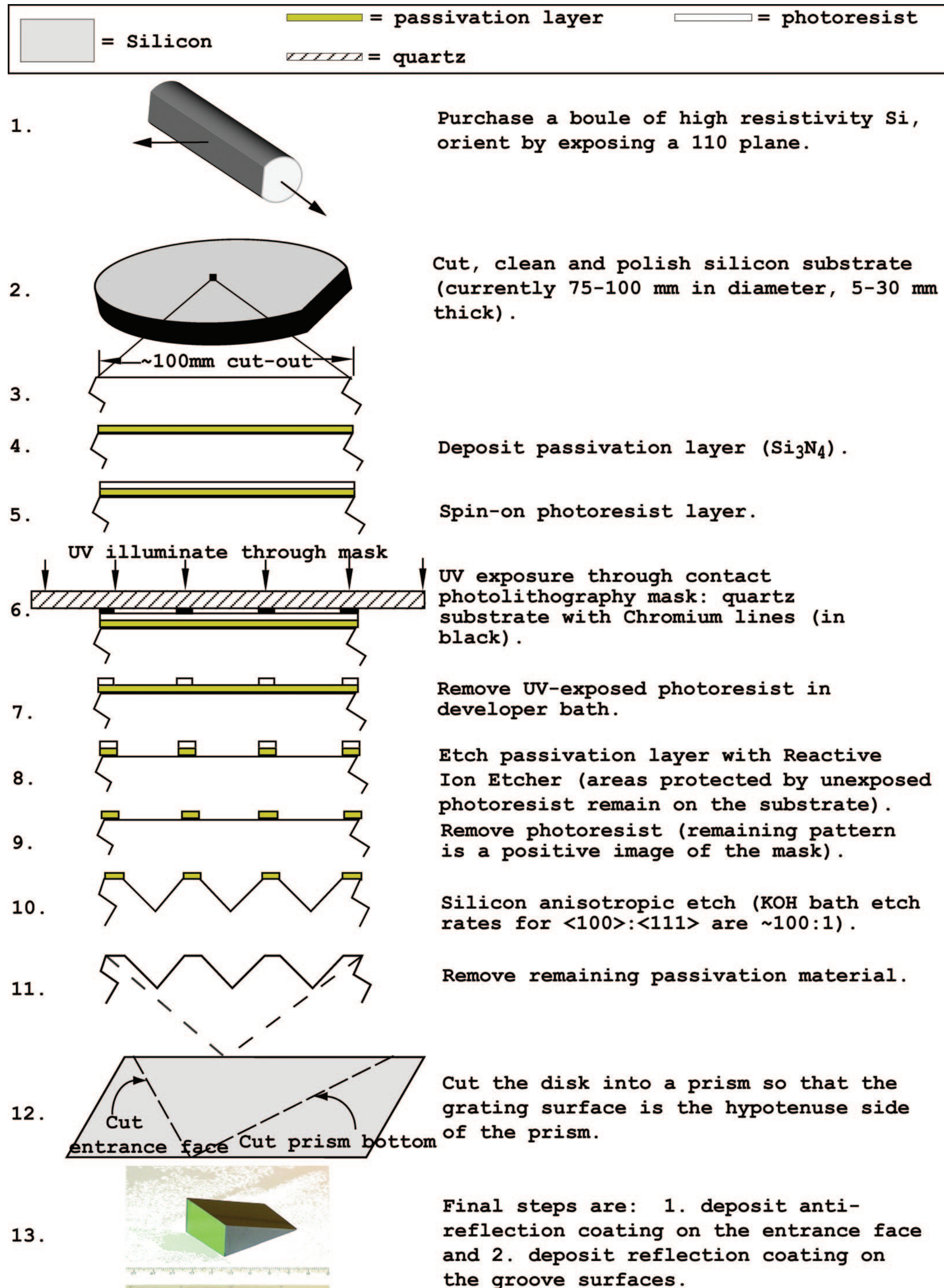

Fig. 3. (Color online) Steps involved in chemically ruling a grating in silicon material.

A. Tolerances

While the increase in the phase difference over the whole illuminated length of the grating attributable to the immersion of grooves in a dielectric works to our advantage by producing a significant increase in the resolving power of the grating, it also imposes stricter tolerances on the groove positioning (see Fig. 1). From the standpoint of sensitivity to manufacturing errors, a silicon immersion grating operating at 2 μm is equivalent to a front-surface device operating at 580 nm. To get an initial estimate of the tolerances at each processing step, we first assume that errors are caused by independent and random misplacements of the individual grooves. These piston errors are distributed with rms amplitude ε_{rms} and produce wavefronts out of phase with the rest of the grating. These wavefronts are not completely able to interfere constructively with the light coming from periodically placed groove facets, and therefore some of the light propagates in undesired directions. In the case of random Gaussian and independent groove displacements, the grating efficiency η for an echelle is given by [46]

$$\frac{\eta}{\eta_0} = \exp\left[-\left(\frac{2\pi}{\lambda}\, 2\varepsilon_{\text{rms}}\right)^2\right], \tag{4}$$

where η_0 is the maximum efficiency possible for a given geometry when no groove displacement errors are present, and ε_{rms} is the rms wavefront error. For $\eta/\eta_0 > 80\%$, the maximum allowable wavefront error is $\varepsilon_{rms} = \lambda/26.6$ (equal to ~22 nm for $\lambda = 580$ nm). Assuming an R2 echelle for which $\delta = 63.4°$, the groove placement error can be up to $\Delta\sigma_{rms} = \varepsilon_{rms}/\sin\delta \approx 25$ nm.

Errors in groove positioning can arise from errors in the substrate flatness, errors in the pattern transfer from the mask to the passivation layer (including errors in the mask itself), and errors in the etching of grooves in silicon. Assuming equal and uncorrelated errors, these steps should each contribute a wavefront error less than $\varepsilon_{rms}/3^{1/2} = 13$ nm. We examine each of these errors and how they translate into manufacturing tolerances. In this example, tolerances are calculated for G1 (blaze angle $\delta = 63.4°$) but formulas are given so the same calculation can be repeated for different blaze angles.

Flatness errors can arise in the disk cutting and polishing steps. The allowable rms error of the surface is (13 nm)/(cos 63.4°) = 29 nm or ~$\lambda/22$ at $\lambda = 632.8$ nm. Note, however, that in polished pieces, the largest deviation from a flat surface usually occurs on large scales and at the edges of the piece, rather than everywhere or on all length scales.

Errors also occur in transferring the unblazed groove pattern to the substrate [4]. Any errors that are present in the pattern on the original photomask will propagate to the grating and result in phase errors with a $\sin\delta$ scaling. Variations in photoresist thickness, passivation layer thickness, and the depth of plasma over etch into underlying silicon substrate will transfer to groove displacement errors with a $\cos\delta$ scaling.

Errors during the chemical etching of grooves into silicon result primarily from spatial variations in the etch rate. The errors arise when etching across the (111) plane shifts the groove positions. The error is the product of ΔR_{111}, the rms deviation from the mean etch rate along the $\langle 111\rangle$ directions and t_{etch}, the time needed to etch a complete groove. If R_{100} is the etch rate in the $\langle 100\rangle$ direction, and h is the groove depth of a symmetric profile with groove spacing σ, then $t_{etch} = h/R_{100}$, where

$$h = \frac{\sigma - \tau}{2} \tan 54.7°, \tag{5}$$

and τ is the length of the groove top. The wavefront error arising from the etching is

$$\varepsilon_{\text{etch}} = \frac{\Delta R_{111}}{R_{100}} \frac{\sigma - \tau}{2} \tan 54.7°. \tag{6}$$

If we want to calculate the etch rate variation allowed for a given wavefront error ε_{etch}, the allowable fractional variation in the $\langle 111\rangle$ etch rate is

$$\frac{\Delta R_{111}}{R_{111}} = \sqrt{2}\varepsilon_{\text{etch}} \frac{R_{100}/R_{111}}{\sigma - \tau}. \tag{7}$$

This result makes high anisotropy ratios, $R_{100}/R_{111} > 100$, desirable. For groove periods of approximately 100 μm and anisotropy ratios of ~100, we need to keep the etching rates constant to within 1% to 2% across the whole surface of the grating.

We have found that the flatness of the entrance face is generally not a source of significant error. Because the light is entering and exiting the substrate along somewhat different paths, combined phase errors in the two transitions through this surface add incoherently and therefore scale with $2^{1/2}(n - 1)$ while the phase errors resulting from reflection scale as $2n \sin\delta$. For a silicon grating with $\delta = 63.4°$, the tolerances for surface accuracy at the entrance face are therefore 1.8 times less stringent than the tolerances for the groove positions. Vendors are capable of delivering surface figures of $\lambda/20$ or better at 632.8 nm for thick silicon pieces.

B. Substrate Preparation

For the work discussed here, we use high-purity float-zone (FZ) silicon boules up to 75 mm in diameter with resistivities of approximately 2000 Ω cm. FZ material has slightly better IR transmission owing to lower O_2 content, and stress birefringence effects, if any, should be minimized [28,47]. The purchased boules were oriented with the $\langle 100\rangle$ axis along the cylinder and had initial length of ~250 mm. Using x-ray diffractometry, a (110) plane was located, and a 38 to 55 mm wide precision flat was machined along the length of the boule. The boule was then mounted and sliced into 1–30 mm thick disks (step 2 in Fig. 3) at 0°, 8.66°, and 22.14° away from the (100) plane toward the (111) planes (but in opposite directions),

corresponding to 54.74°, 63.4°, and 32.6° blaze angles of G0, G1, and G3. All orientations were made with a precision of ~0.05°. Errors larger than this in the (110) orientation result in groove defects such as dislocations in the groove walls [48]. Tilting the boule relative to the (100) plane during the dicing produced asymmetric disks, which are awkward to spin coat with photoresist.

The asymmetric disks were ground on one side and then polished using the chemical mechanical polishing (CMP) method to avoid subsurface damage to the crystal lattice. The flatness of silicon substrates was measured interferometrically by the polisher. Over the central 86% of the area of the 75 mm diameter disks, the measured rms error of the polished silicon surface was smaller than $\lambda/100$ at 632.8 nm for all disks.

Polished substrates were coated with a passivation layer (Table 1 and step 4 in Fig. 3). We have used both silicon dioxide and silicon nitride in our processing, but favor Si_3N_4 because of its negligible etch rate in KOH solutions. For SiO_2, the large etch rate of 100 nm/hr in KOH [49] leads to defects in the mask layer and, subsequently, in the groove wall [5,50]. The oxide must be thick enough not to etch through while the KOH produces the grooves leading to a typical oxide thickness of 600 nm. During the thermal growth of the SiO_2 layer at high temperatures (typically above 1000 °C), oxygen diffuses into silicon crystal, thus increasing the amount of impurities that can cause etch pits during the chemical etching of grooves. Because we wanted to use thinner passivation layers and avoid high-temperature processing steps, we started using low-pressure chemical vapor deposition (LPCVD) nitride. A nitride layer of 60–100 nm thickness can have thickness uniformity of <5% peak to valley over the whole surface, well within our tolerance for substrate flatness. The thickness of the passivation layer also affects the groove positioning errors. Thicker passivation layers tend to cause larger transfer errors, thus diminishing grating performance [4].

C. Pattern Transfer

Before starting processing, each piece is cleaned with acetone, isopropanol, methanol, and distilled water. After drying with a stream of dry nitrogen gas, they are baked for 1 h. We use contact masks consisting of several hundred to several thousand parallel chrome lines (a few micrometers wide by 50 to 100 mm long) on quartz substrates to define the pattern that needs to be transferred to the passivation layer. The commercially obtained VLSI photolithographic masks are patterned onto 6 in. square quartz substrates up to 0.25 in. thick. These masks are flat to better than $\lambda/20$ at 632.8 nm, as shown by the regularity of the fringe patterns that appear when the masks are placed in contact with the silicon substrate or with an optical flat. The original mask is more than adequately accurate. The vendor performed measurements of line positions on a random sample of lines on completed masks. The measured rms errors in line placement (relative to the first measured line) were 5 nm and 10 nm, respectively, for the masks used to make G1 and G3.

The first step in the pattern transfer involves the deposition of a uniform layer of photosensitive organic emulsion (photoresist) on top of the passivation layer (step 5 in Fig. 3): we spin the substrate up to 3500 rpm to spread an adhesion layer of primer and a novolak photoresist over the surface. The uniformity of primer and photoresist can be verified during this step by observing the color change across the substrate attributable to reflection from silicon and interference inside the photoresist layer. The measurements using an ellipsometer confirm that the achieved photoresist thickness, 500 ± 50 nm agreed with the manufacturer specifications, and the uniformity of the photoresist coated surfaces was better than 1 nm in all cases. We harden the photoresist by baking and are then ready to expose the desired line pattern.

In the next step, the line pattern is transferred to the photoresist by exposure to UV radiation (step 6 in Fig. 3). We align the mask so that the lines are perpendicular to within 0.05° of the (110) precision flat of each disk. The mask is brought into contact with the photoresist and illuminated by i-line ($\lambda = 365$ nm) collimated UV radiation from a mercury lamp. Our custom UV-exposure system insures uniform illumination by moving the substrate through a narrow, well-baffled illuminated strip. The substrate is removed from the UV aligner apparatus and immersed in a commercial developer, resulting in a positive image of the mask in photoresist.

The next step is the transfer of the mask image formed in photoresist down to the SiO_2 or Si_3N_4 passivation layer (step 8 in Fig. 3). For SiO_2 passivation layers, we immerse the substrate in a buffered oxide etch (BOE), which removes SiO_2 between the photoresist lines. The resulting SiO_2 stripe profile is not rectangular but rather bowl-shaped as a result of an isotropic etching of SiO_2 in a BOE solution. The spacing between the stripes will be maintained as long as temperature and chemical concentrations are uniform across the surface of the substrate. The isotropic etching of SiO_2 in BOE and KOH solutions sets a fundamental limit on the minimum width of mask lines, as they have to be sufficiently wide to withstand both etches. For Si_3N_4 passivation layers, we use a reactive ion etcher (RIE) to remove exposed portions of nitride, leaving intact the stripes of nitride that are protected by unexposed photoresist. The industrial RIE machine we used is optimized for thin wafers (up to a few millimeters thick), so we used focusing rings to keep the plasma density uniform across the surface. Overetch into silicon is another possible source of groove positioning error. While thick pieces are expensive for individual step tests, we can estimate the magnitude of overetch indirectly. We have tuned the duration of the RIE etch step to within 10% of the actual value, so the maximum depth of overetch in silicon is the equivalent of 6 nm for a 60 nm thick layer of Si_3N_4. The selectivity (etch

rate of Si_3N_4/etch rate of silicon) is at least 2 for our process recipe. The average overetch into silicon crystal is 3 nm, and the variation across the surface is some fraction of this value and negligible. After RIE, the remaining photoresist is stripped in acetone (step 9 in Fig. 3), leaving parallel stripes of SiO_2 or Si_3N_4 on a pure silicon substrate. These stripes serve as a mask for the anisotropic etch that creates the grooves.

D. Etching Grooves

We blaze the grating by etching grooves into the silicon using an aqueous KOH solution (step 10 in Fig. 3). V-shaped grooves in silicon are a result of anisotropic etching of silicon through a mask of parallel lines. For aqueous KOH, the ratio of (100):(111) rates can be as high as 400:1 [51]. To produce a good grating, we must minimize errors in groove spacing over a large area. As indicated by Eq. (7), a high anisotropic etch ratio minimizes the contribution to groove positioning errors by uneven undercutting of the {111} surfaces. Empirical etch rates in aqueous KOH solutions vary widely in the literature [49]. We therefore measured our own rates for both symmetric and asymmetric groove profiles and found that they are almost identical. Our KOH etching apparatus maintains the etchant temperature at a constant 68 °C and provides ultrasonic agitation. We add isopropanol, which serves as a surfactant [52] to the aqueous KOH. The etching reaction, which takes place in several steps, can be summarized as follows [53]: $Si + 2OH^- + 2H_2O \rightarrow SiO_2(OH)_2^{--} + 2H_2$. The H_2 bubbles formed in this reaction can block small areas on the surface of the crystal and lead to microroughness. The isopropanol and the ultrasonic vibrations promote the quick detachment of hydrogen bubbles and result in smooth surfaces [52]. After etching, the substrate is rinsed in distilled water.

We have produced gratings on large silicon disks with various blaze angles and groove periods (see Fig. 3 of [1]). We use both scanning electron microscopy [(SEM), Fig. 4] and profilometry to measure etch rates and anisotropy ratios so that we can fine-tune the etch times for a given temperature and KOH concentration. We determined etch rates from SEM images by measuring the etched depth in the $\langle 100 \rangle$ and $\langle 111 \rangle$ directions on incomplete samples and dividing each by the etch time (see Fig. 4). Our measurements result in $R_{100} = 28 \pm 0.5$ μm/hr, and $R_{111} = 0.46 \pm 0.1$ μm/hr. The measured anisotropy ratio is $R_{100}/R_{111} = 60$. Because the etch rate R_{111} is nonzero, the angle at the groove bottom differs from the ideal 70.5° (see Fig. 5). We can also determine the anisotropic etch ratio by measuring the vertex angle with a profilometer, corrected for stylus arm arcing. We obtain an anisotropy ratio $R_{100}/R_{111} = 69$, in agreement with the value determined from the SEM measurement of the mask undercut. In order to attain the desired blaze angle, the finite value of the etch rate R_{111} must be taken into account during the design and material cutting. For example, after etching grating G1 for 2 h, the blaze angle has changed from 63.4° to approximately 62.6°. At 2 μm in immersion, when the grating operates in the 247th order,

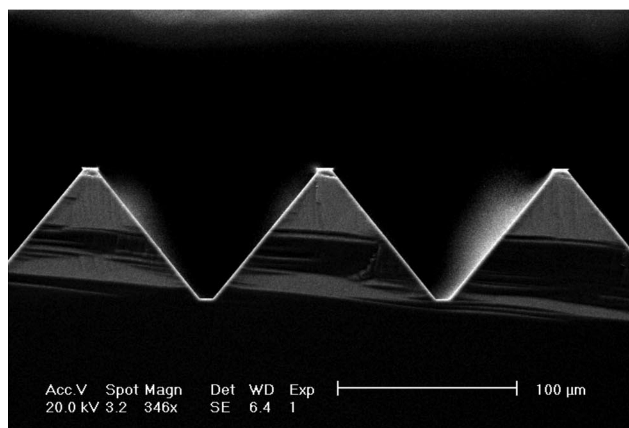

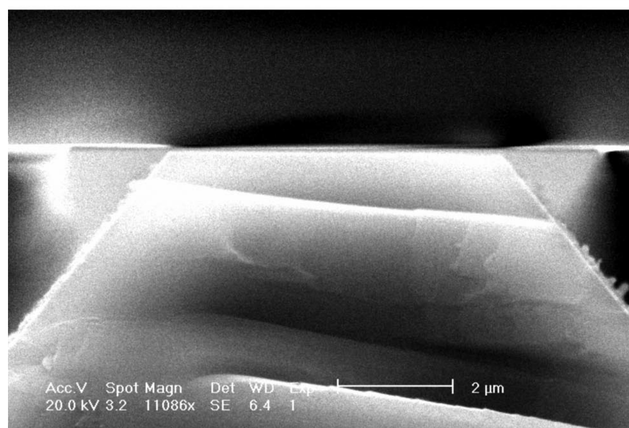

Fig. 4. We used scanning electron micrographs of etched gratings to determine etch rates R_{100} and R_{111} for (100) and (111) planes. R_{100} is calculated from an incompletely etched sample (top micrograph) by measuring the depth from the top and dividing by the etch time. R_{111} is determined from the bottom micrograph by measuring the length of the undercut silicon nitride layer and multiplying that length by sin 54.7°.

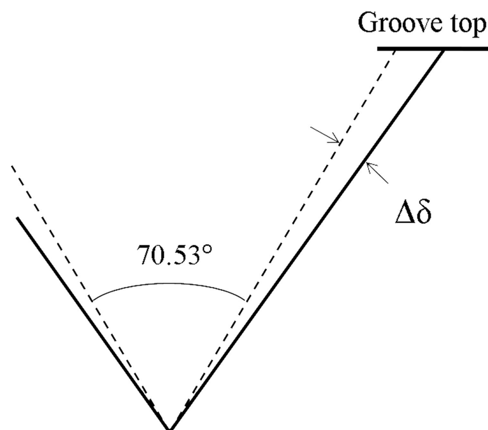

Fig. 5. Material at the top of the groove is exposed to the etchant for longer than the material near the vertex. As a result, the opening angle of the groove increases with time causing a change in the blaze angle.

the blaze wavelength will shift from the predicted 1.998 μm for $\delta = 63.4°$ to 1.984 μm for $\delta = 62.6°$, a shift of −0.014 μm that puts the original blaze wavelength in order 245.

E. Shaping and Coating

When the blazed grating is complete, we strip the remaining passivation layer (step 11 in Fig. 3). Silicon dioxide is removed using a 4% buffered hydrofluoric acid solution, and silicon nitride is removed using a concentrated phosphoric acid solution (85%) heated to close to its boiling point (158 °C). At 150 °C, phosphoric acid etches silicon nitride at 1–2 nm/min while silicon is unaffected [54]. The phosphoric solution also removes polymer formations of $Si(OH)_4$, which are by-products of the KOH etch and tend to settle near the groove top (see Fig. 6). Removing the polymer formations decreases scattered light by allowing for an unbroken deposition of a reflective coating.

After the stripping step, the device is shaped into a prism with the grating covering the hypotenuse (step 12 in Fig. 3) using custom jigging provided by the vendor to hold the piece and protect the grating surface. The entrance face is surface ground and then optically polished to a surface figure of λ/20 or better at 632.8 nm. We tilt this face by a small amount off parallel with the groove surface (usually 1° in the cross-dispersion direction). Without such a tilt, residual reflected light from the entrance face propagates in the same direction as diffracted light at the blaze wavelength of each order. For grating G1, we also wedged the bottom of the prism in order to redirect

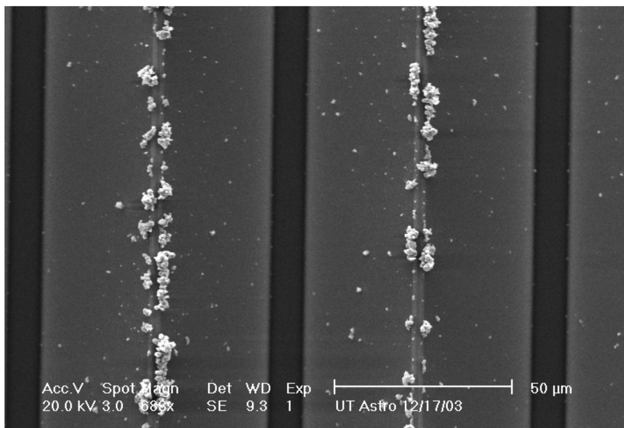

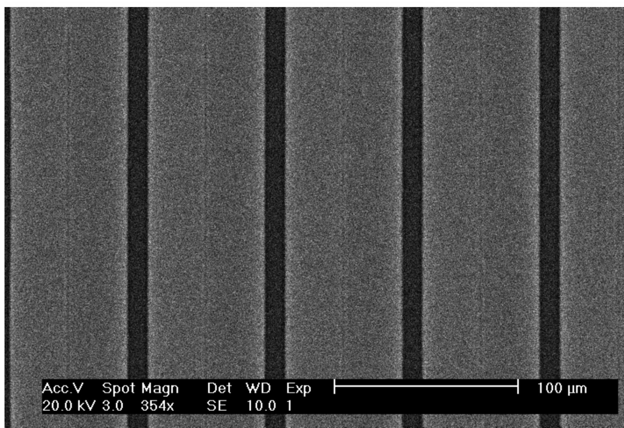

Fig. 6. (Top): Scanning electron micrograph of a grating etched on a thin wafer showing thin strips of residual passivation layer. A by-product of KOH etching, $Si(OH)_4$, polymerizes and creates white grains. (Bottom): The same grating after etching in hot phosphoric acid. Both the nitride strips and the etch residue are removed by the phosphoric acid.

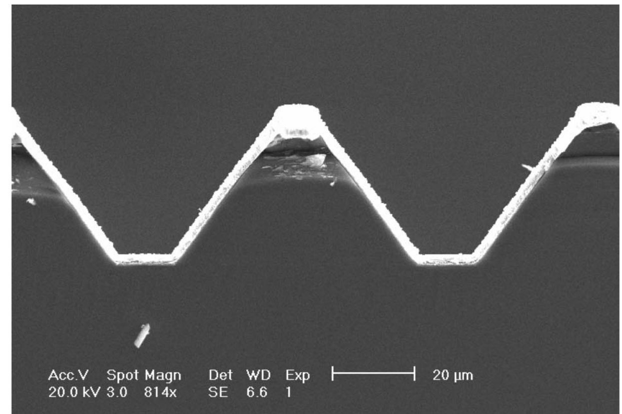

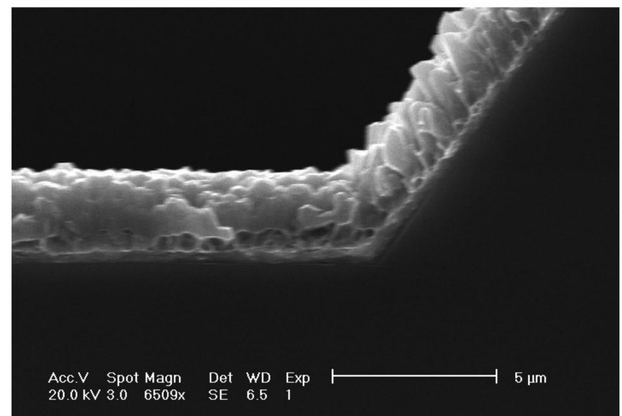

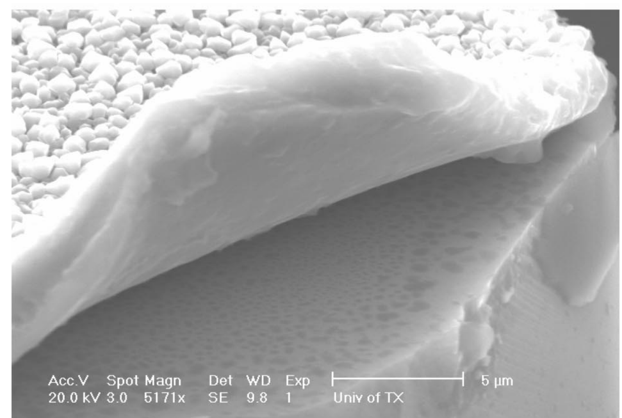

Fig. 7. (Top): Scanning electron micrograph of an aluminized grating showing several grooves and (middle) a corner detail of one groove. The grating is incompletely etched. (Bottom): A corner of the aluminum layer peeled back by many rapid thermal cycles reveals the smoothness of the aluminum layer in contact with the silicon surface.

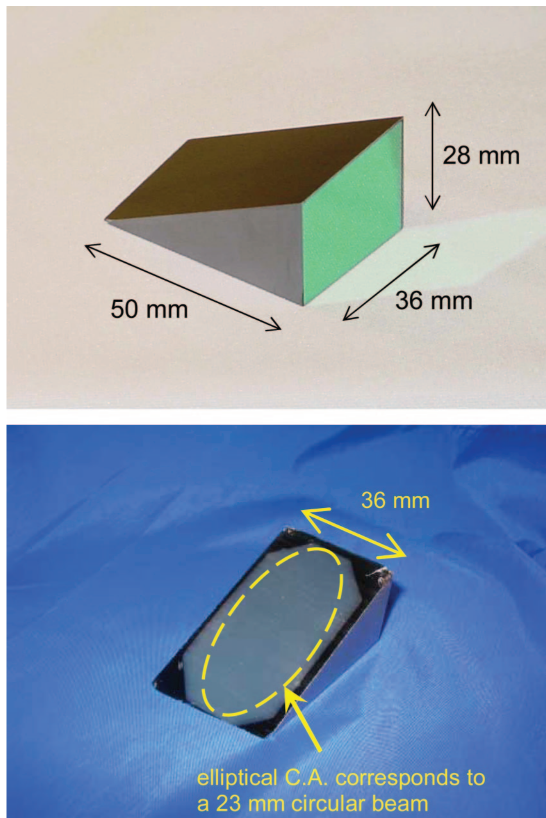

Fig. 8. (Color online) (Top): Grating G1–shaped to its finished prism form, with a 1.2–5 μm antireflection coating on its entrance face. (Bottom): Grating G1 after an aluminum coating was deposited on the grating surface. The ellipse drawn on the grating illustrates the boundary of a 23 mm circular beam from the entrance face, projected on the grating surface.

diffracted light from the ends of the orders, which may hit the bottom of the prism.

We applied a commercial antireflection coating on the entrance faces of gratings G0 and G1. The coating was optimized for transmission from 1.1 to 5 μm. The quality of both coatings was very good with a maximum reflectivity of 10% at 1.5 μm and reflectivities below 3% between 1.6 and 5 μm. A metallic overlayer was applied to the groove surfaces to enhance the internal reflectivity of the grooves (Fig. 7). We selected sputtered aluminum for this overlayer because of the ease of depositing relatively thick (2 μm) layers without voids [6]. Repeated rapid cycling between 290 and 77 K shows that the aluminum coating adheres well and is robust against thermal shock (see Fig. 7). Figure 8 shows the completed grating G1.

3. Measured Performance of Completed Gratings

Once we complete a grating, we visually inspect it for surface damage such as scratches and defects in the groove pattern. We then conduct optical tests of the wavefront shape and error, the point-spread function (PSF), and the efficiency of our gratings. This analysis feeds back as improvements to our production process.

A. Imaging/Visual Confirmation of Our Process

We use profilometry to verify the groove shape and SEM to verify groove shape, size and orientation, and to estimate the number and type of surface defects. This testing is possible only on small wafer samples since the vertical clearance inside the SEM chamber is only a few millimeters. We can also observe any larger defects in etched substrates with an optical microscope.

B. Efficiency

We measure grating efficiency using monochromatic spectra. Monochromatic light is diffracted into discrete orders given by the grating equation [Eq. (2)]. The blaze function determines the intensity distribution among the diffracted orders (Figs. 9 and 10). For

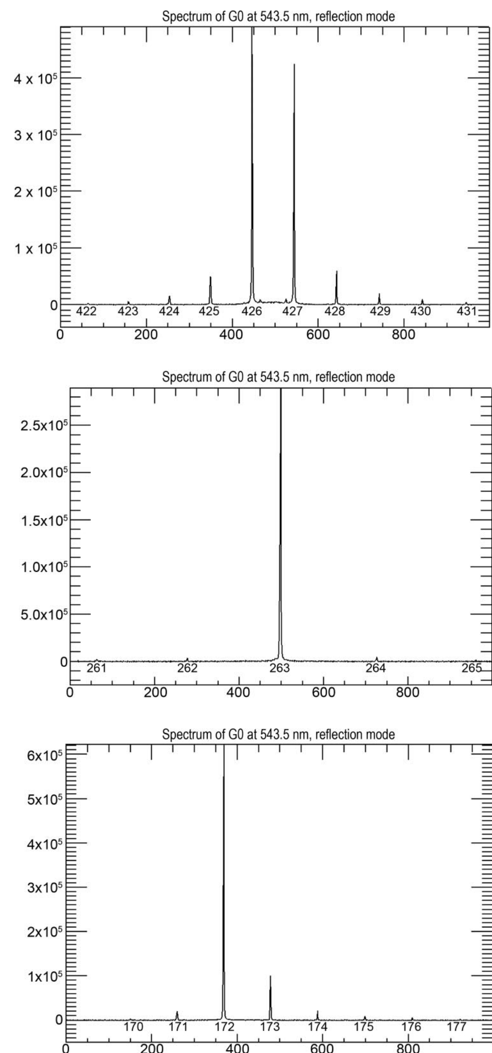

Fig. 9. Front-surface, monochromatic spectra of (top) G0, (middle) G1, and (bottom) G3 at 543.5 nm. The lower scale on the x axis gives the position along the spectrum in pixels while the upper scale identifies the order number of the peaks. The y axis scale is in counts integrated over several rows in the cross-dispersion direction. The gratings show a steady improvement in eliminating scattered light and ghosts going from the earliest work (G0) to our most recent effort (G3).

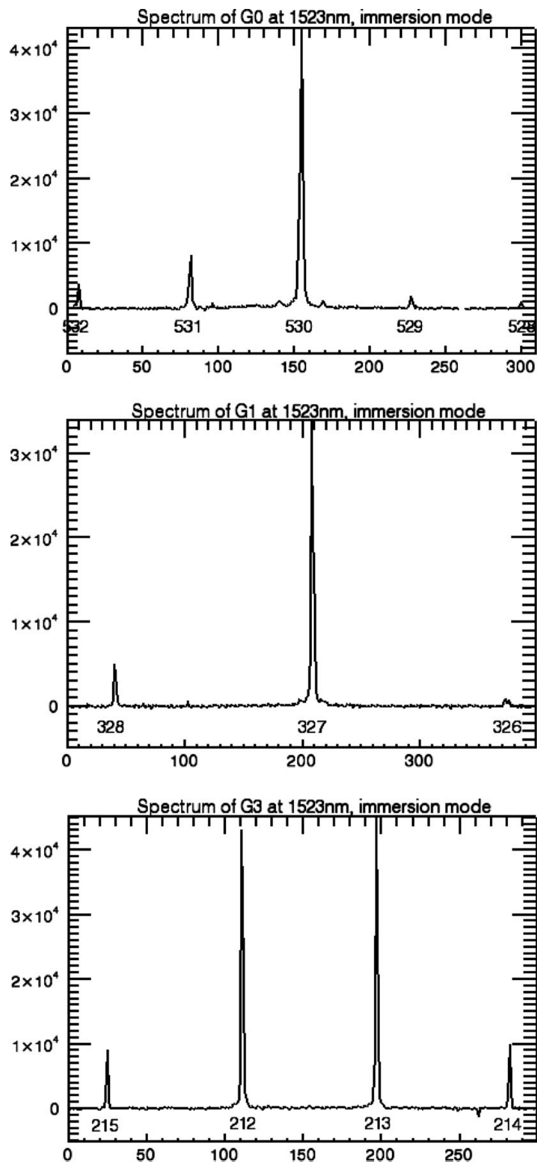

Fig. 10. Monochromatic spectra of (top) G0, (middle) G1, and (bottom) G3 in immersion at 1.523 μm. The lower scale on the x axis gives the position in pixels while the upper scale identifies the order number of the peaks. The y axis scale is in counts integrated over 10 rows in the cross-dispersion direction.

high-order echelle gratings, the angular distribution of the blaze envelope approaches

$$\frac{I(\beta)}{I_0} = \left(\frac{\sin\left[\frac{\pi s}{\lambda}(\sin\beta - \sin\alpha)\right]}{\left[\frac{\pi s}{\lambda}(\sin\beta - \sin\alpha)\right]} \right)^2, \tag{8}$$

where s is the effective groove width [55]. The peak intensities of each diffracted order match this blaze envelope at each β for which there is a valid solution of the grating equation. For gratings operating in the high orders where Eq. (8) is valid, we can use the equation to correct the measured efficiency at the wavelength of the monochromatic source to the efficiency in the peak order at the blaze wavelength.

Our test setup consists of two bench spectrographs [5], one of which uses two visible (λ = 543.5 and 632.8 nm) He–Ne lasers and a second, which uses an IR (λ = 1.523 μm) laser to illuminate the grating in collimated light. For visible light, the beam size was 15 mm for G0 (limited by the size of the grating) and 25 mm for G1 and G3. For the IR setup, the beam size was 10 mm (limited by optics). Using beam splitters, we were able to observe a reference mirror over a light path almost identical to that of the grating and measure return signals from both simultaneously. Light from the test grating and the reference mirror is focused onto an optical CCD or an InGaAs IR detector array to record the monochromatic spectrum. To focus the spectrum onto the detector arrays, we use either an f = 125 mm (for the IR setup) or f = 200 mm (for the visible setup) lens to record a series of 2–10 orders on the detector, or an f = 838 mm lens to resolve the diffraction spot and analyze the grating PSF. Figures 9 and 10 show monochromatic spectra. At 543.5 and 632.8 nm, the gratings are used as front-surface devices. At 1.523 μm, gratings are used as immersion echelles. We used two types of reference mirrors: silicon for uncoated gratings at optical and IR wavelengths and gold for coated gratings measured in immersion.

Table 2 gives the results of the efficiency determinations for G0, G1, and G3. The third column lists the

Table 2. Measured Immersion Grating Efficiencies Obtained From Reflection Measurements at λ = 543.5 and 632.8 nm and Immersion Measurements at λ = 1523 nm

Grating	Mode[a]	$\eta_{measured}$	η_o	$\eta_{groove} = \eta_{measured}/\eta_o$	$\eta_{relative}$
		λ = 543.5 nm[b]			
G0	U, SiR, RG	63%	91%	69%	60%
G1	U, SiR, RG	63%	88%	72%	62%
G3	U, SiR, RG	78%	91%	86%	74%
		λ = 632.8 nm[b]			
G0	U, SiR, RG	62%	91%	68%	59%
G1	U, SiR, RG	64%	88%	72%	62%
G3	U, SiR, RG	78%	90%	87%	75%
		λ = 1523 nm[c]			
G0	C, AuR, ImG	48%	85%	56%	45%
G1	C, AuR, ImG	64%	86%	74%	59%
G3	U, SiR, ImG	40%	46%	88%	71%

[a]Abbreviated overview of conditions under which efficiency measurements were performed. U–uncoated grating, C–grooves coated with aluminum, entrance face coated with an antireflection layer, SiR–silicon reference mirror, AuR–gold reference mirror, RG–measurement in reflection mode, ImG–measurement in immersion mode.

[b]Relative efficiencies at visible wavelengths assume that the silicon is perfectly reflecting.

[c]Relative efficiencies in immersion. Note that at 1.523 μm in immersion, the antireflection coating has a measured loss of 5.5% per pass, and the predicted reflection loss at the silicon–aluminum boundary is 7%.

measured efficiency, $\eta_{measured}$, which is simply the sum of the signal in the monochromatic orders observed on the detector, divided by the signal from the reference mirror. There are two types of derived efficiencies that can be obtained from this measured value. The groove efficiency, η_{groove}, is relevant to evaluating the quality of the grating grooves and groove placement. The relative efficiency, $\eta_{relative}$, is useful in predicting the ultimate throughput of an instrument using a micromachined front surface or immersion echelle and is directly comparable to the relative efficiencies quoted for commercial echelle gratings.

The groove efficiency, η_{groove}, is obtained from the measured efficiency $\eta_{measured}$ by correcting for all effects related to the grating geometry and any coatings on the device, but not for effects resulting from imperfect blazing or mispositioning of the individual grooves. We derive η_{groove} by normalizing $\eta_{measured}$ by a calculated geometric ideal efficiency correction factor η_o. This correction factor contains terms that result in a value of η_{groove} that gives the efficiency of a given grating relative to one with the same groove spacing and filling factor for the blazed facets, but with perfectly reflecting, perfectly positioned grooves with perfectly smooth surfaces. We calculate η_o for each grating and observing geometry (front surface or immersion) at a given wavelength and list the values in Table 2. For all gratings, η_o includes a term to account for the mismatch between the blaze function minima and the interference maxima for orders above and below the blaze order. This mismatch is most severe for grooves that do not fill the spacing between them but is also present when the filling factor is 1, even up to very high order. It causes light loss into adjacent orders [56]. The value of the mismatch term was determined by calculating the positions and intensities of all propagating orders and dividing the sum of intensities for orders we were able to observe by the sum of all intensities in propagating orders. For visible wavelengths, where the gratings are used as front-surface devices, there is an additional term to account for the incident light blocked by the groove tops (which have no effect in immersion). For IR wavelengths, where the gratings are used in immersion, there is an additional term to properly account for losses incurred as the light enters and exits the silicon prism. To determine this term, we measured the transmission of uncoated and antireflection coated silicon witness samples.

The fourth column of Table 2 gives the value of η_o, and the fifth column gives $\eta_{groove} = \eta_{measured}/\eta_o$. The groove efficiency has steadily improved from our first results with G0 through our newer devices G1 and G3. The good agreement between the values of η_{groove} determined from front-surface measurements in the optical and from measurements at a comparable effective wavelength in immersion show that we can account correctly for geometric effects and losses at the silicon–air interface and use front-surface measurements to predict accurately the ultimate performance of a given grating in immersion. The small differences for G0 most likely reflect differences in performance across the grating surface.

To determine the relative efficiency of a grating on the blaze ($\eta_{relative}$, given in column 6 of Table 2), we need to correct $\eta_{measured}$ to give us the intensity of the return signal for monochromatic light at the wavelength corresponding to the peak of the blaze, relative to the signal from the comparison mirror. We use the method of [56] to calculate the shape of the blaze

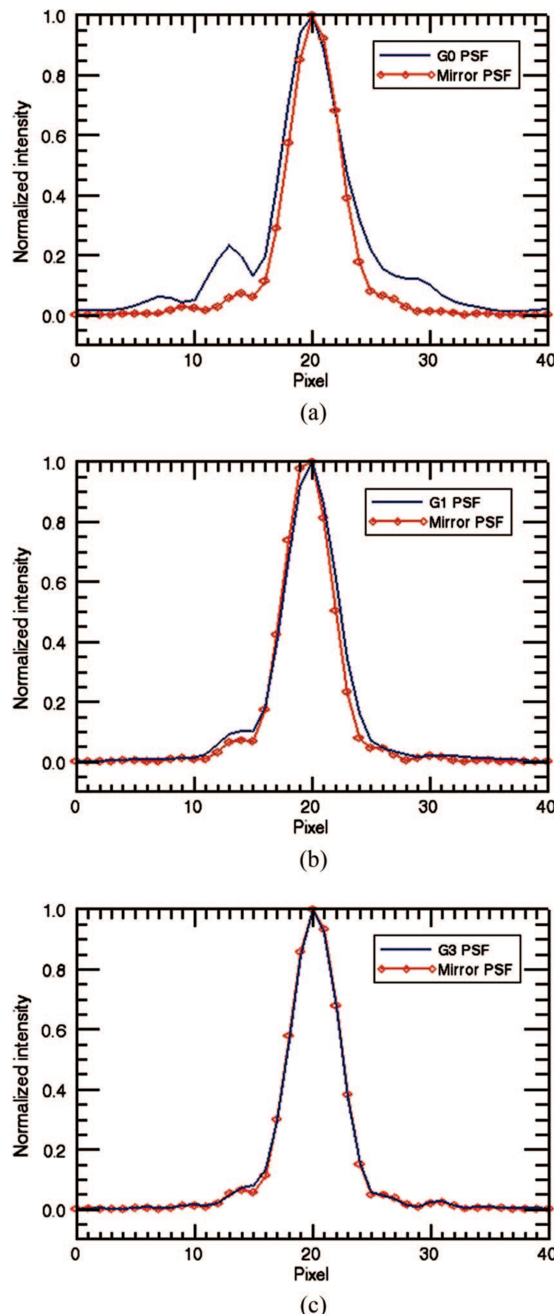

Fig. 11. (Color online) Spectral PSFs of (a) G0, (b) G1, and (c) G3 compared to the PSF of a mirror. All profiles were measured in immersion at 1.523 μm with a 10 mm collimated beam (see Table 3). The wings on the profiles of G1 and G3 reflect the collapse of the Airy rings to one dimension.

envelope for the geometry of each grating, calculate the correction factor to go from the measured signal in the orders striking the detector array to the total signal over all orders, calculate the correction factor to go from the total signal to the signal in the order at the peak of the blaze function, and scale $\eta_{measured}$ by the product of these two factors to derive $\eta_{relative}$ in Table 2.

The relative efficiencies measured for G1 and G3 in the visible are comparable to or exceed the best throughput values quoted for commercial front-surface echelle gratings, despite the losses caused by the groove tops. More significantly, the relative efficiencies of G1 and G3, measured in immersion at 1.523 μm, near the short end of their useable range, also exceed the efficiencies of commercial echelles, this despite having been measured at a wavelength where the broadband antireflection coatings on the gratings were particularly bad (we have a total loss of ~11% for the two passes through the entrance face). In fact, most of the departure from unity transmission at 1.523 μm can be attributed to the antireflection coatings. The entrance face of G3 is uncoated. To facilitate a comparison between the relative efficiencies of G1 and G3, in Table 2 we have corrected the G3 value for the dielectric loss at the air–silicon interface by assuming a coating with the same value of reflection loss as that for the antireflection coating on G1.

C. Resolving Power and Point-Spread Function

We measured the 1.523 μm PSF of G0, G1, and G3 directly in our bench spectrometer setup with a 10 mm beam, the maximum size allowed by our beam splitter (see Fig. 11). The first step in analyzing the images was to fit a 2D Gaussian function in order to measure the width of the diffraction spot. The results of this step are summarized in Table 3. The predicted resolving power, $R_{predicted}$, is calculated using Eq. (1). The demonstrated resolving power, $R_{demonstrated}$ was calculated using the angular dispersion relation for immersion gratings used in the Littrow mode,

$$\frac{d\beta}{d\lambda} = \frac{2n \tan \delta}{\lambda}, \quad (9)$$

and corrected for pixel sampling. From this equation, we can calculate

$$\Delta\lambda = \frac{\lambda}{2nf \tan \delta} \Delta x, \quad (10)$$

where $\Delta x = 30\ \mu m \times FWHM_x$ (in pixels), and $R_{demonstrated} = \lambda/\Delta\lambda$. We demonstrate a resolving power of 75,000 at 1.523 μm using grating G1. Some of the difference between the predicted and measured resolving powers arises because of the slight taper of the electric field distribution of the 10 mm aperture.

Figure 11 shows 1D spectral PSFs, produced by summing over 10 pixels in the cross-dispersion direction. Gratings frequently work below the diffraction limit. Our efficiency measurements were done at $R \ll R_{diff}$. The resolving power measurements show that our gratings can perform at R_{diff} up to 80,000. The Strehl ratio is the measure of diffraction-limited performance. It is defined as the peak value of the PSF in the observed image relative to its value for an unaberrated image (with both PSFs normalized to the same total power). A system with a Strehl of more than 0.8 would have an rms wavefront error of λ/14 or less. In practice, we calculated the area under the 1D spectral PSF for each grating and normalized the PSF by the ratio of that area to the area under the mirror PSF, which is in this case our unaberrated PSF. The peak value of the normalized grating PSF is the Strehl ratio. Table 3 gives the Strehl ratios for gratings G0, G1, and G3, including values measured directly from the IR spectra in immersion and values calculated from the wavefront errors determined from optical interferograms (Fig. 12). The two types of Strehl measurements agree well, except in the case of G0, probably because the quality of G0 varies across the surface and depends strongly on which part of the grating surface is used. The performance of G1 and G3 is diffraction limited at 1.523 μm when they are used as immersion gratings. The high Strehl over a 25 mm beam measured for G1 and G3 indicates that they should achieve resolving powers 2.5 times larger than those listed in Table 3. Over some areas of its surface, G0 is diffraction limited at 2 μm. The agreement between the front-surface tests using optical interferometry and the direct immersion tests, together with the measurements of periodic errors (discussed in Subsection 3.D.3), demonstrate that front-surface measurements, both spectroscopic and interferometric, can accurately predict the performance of echelles in immersion.

Table 3. Width of Point-Spread Function (PSF) and Measured Resolving Power

Grating	$FWHM_x$ (in Detector Pixels)	$FWHM_y$ (in Detector Pixels)	$R_{demonstrated}$	$R_{predicted}$	Strehl Ratio: From IR PSF[a]	Strehl Ratio: From Interferogram[b]
Mirror	4.78	4.90				
G0	5.99	5.11	45,500	64,100	0.71	0.82
G1	5.10	4.79	75,400	90,500	0.91	0.90
G3	4.74	4.90	26,000	28,900	0.99	1.00

[a]Measured over a 10 mm diameter beam.
[b]Measured over a 15 mm diameter beam for G0 and a 25 mm beam for G1 and G3.

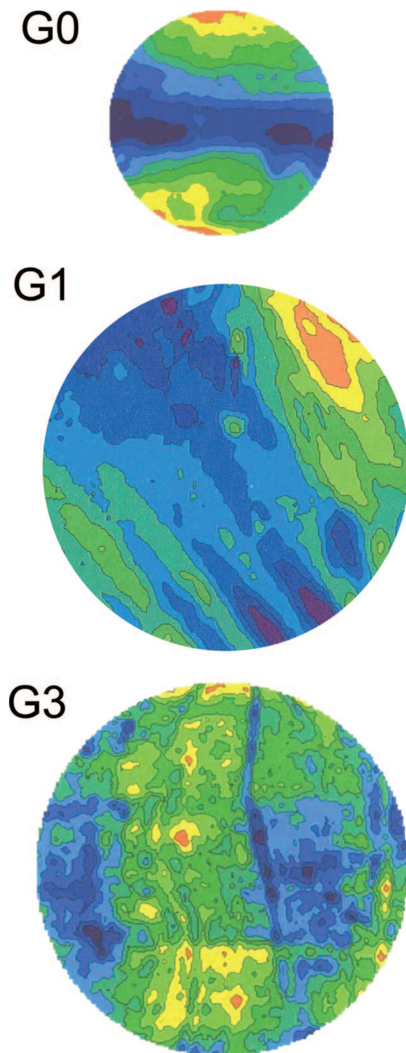

Fig. 12. (Color online) Surface error plots of grating surfaces of G0 (beam diameter 15 mm), G1, and G3 (25 mm) taken with a Zygo interferometer using $\lambda = 632.8$ nm, before the devices were shaped into prisms. From top to bottom, the peak-to-valley ranges are 0.2894, 0.2627, and 0.0572 waves, and the rms wavefront errors are 0.0682, 0.0522, and 0.0099 waves, respectively. Each contour corresponds to 10% of the individual peak-to-valley range. All three gratings exhibit diffraction limited performance on the scales shown.

D. Wavefront Aberrations and Grating Defects

Errors in the groove shape and spacing and surface roughness degrade the performance of diffraction gratings by lowering the optical efficiency and causing unwanted features in the observed spectra. In general, these errors manifest themselves as ghosts, satellites, grass, and diffuse scatter [57]. We discuss our measurements of these errors, as well as ways to improve the performance of future gratings.

1. *Grass*

Groove position errors displace the grooves off a common phase plane, lessening the coherence of the diffracted signal. When these errors are random, they produce "grass," i.e., scattered light that appears between orders in a monochromatic spectrum. The intensity of light in grass, I_{grass}, is given by [57]

$$\frac{I_{grass}}{I_0} = \left(\frac{2\pi}{\lambda}\, 2\varepsilon_{spacing} \sin\delta\right)^2, \tag{11}$$

and the measured values of this ratio for G0, G1, and G3 are listed in Table 4. Equation (11) is an approximation derived from Eq. (4) for small values of $\varepsilon_{spacing}$. From the measured value of I_{grass}, Eq. (11) allows an estimate of $\varepsilon_{spacing}$, that is, the portion of the spacing error we can assign to random displacements of groove positions. The intensity distribution of grass matches that of the blaze function determined by the diffraction of a single groove [58]. We estimated the fraction of light η_{grass} in the grass from our monochromatic spectra by integrating over 10 to 20 rows of the images to obtain a 1D spectrum, and then subtracting out previously determined efficiency $\eta_{measured}$ in observed orders as well as any observed ghosts. The angular range of integration in the cross-dispersion direction was only 0.07°, so any diffuse scattered light should not contribute significantly. The random spacing errors, $\varepsilon_{spacing}$, derived from the observed grass intensity are both very small and close to the same value for all three gratings (see Table 4). This result implies that we have good control over the pattern transfer process and good repeatability, even for thick silicon substrates. G0 has a somewhat larger rms error, which can either be the result of using a SiO_2 layer as the etch mask or the result of intrinsic errors in the mask (or both). The scattered light in grass of our most recent grating G3 (see Fig. 13) is comparable to the level measured for a commercially produced R2 echelle used in the 2D Coudé spectrograph on the 2.7 m telescope at McDonald Observatory [59].

Table 4. Scattered Light Due to Random Errors in Groove Positions

Grating	I_{grass}/I_0	$\varepsilon_{spacing}$ [a]	ε_{phase}	$\varepsilon_{spacing}$ from Interferograms [b]
G0	7.9%	17 nm	14 nm	43.2 nm
G1	4.6%	12 nm	11 nm	33.0 nm
G3	1.9%	13 nm	6.9 nm	6.3 nm

[a] Calculated from I_{grass}/I_0 using Eq. (11).
[b] The rms displacement error over areas shaped and sized to match the area used in the spectroscopic measurements for which $\varepsilon_{spacing}$ was determined. The slightly larger value of $\varepsilon_{spacing}$ for G0 likely reflects the use of a SiO_2, rather than a Si_3N_4, etch mask and the use of a ruled mask during the photolithography step.

The total measured errors derived from the optical interferograms (column 5 of Table 4) by calculating the distance equivalent of the rms deviation of the phase fronts, are larger than the spacing errors and differ more strongly from grating to grating (see Table 4). As we will show, these larger values derived for G0 and G1 result from repetitive errors, which produce ghosts rather than grass.

2. *Diffuse Scattered Light*

Small scale (micro) roughness (scale sizes less than λ) of the groove surfaces causes incident light to scatter.

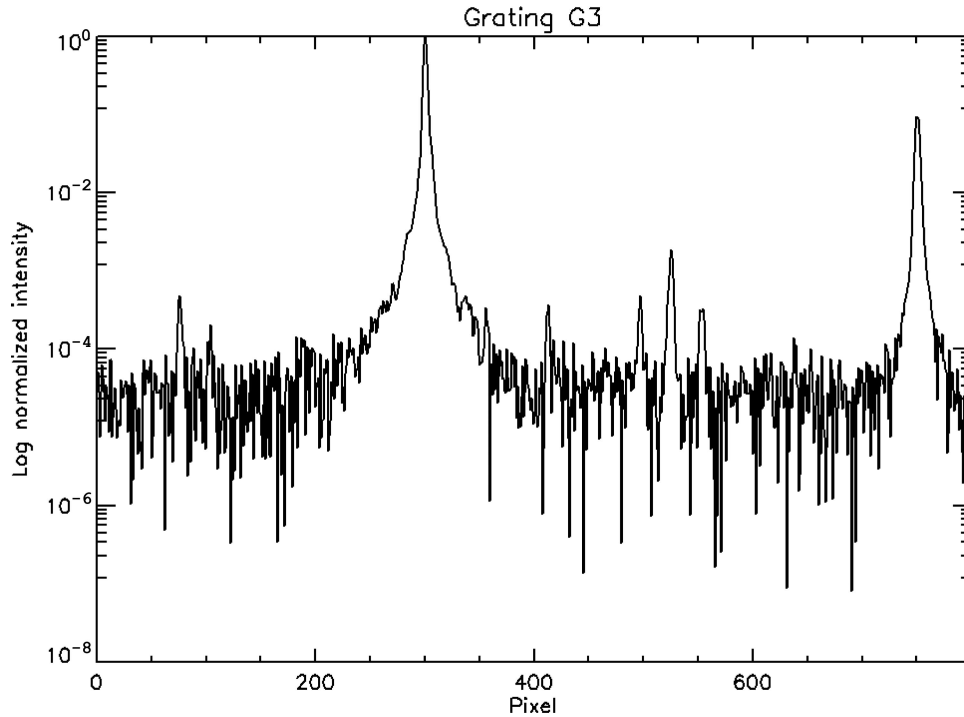

Fig. 13. Sum of several thousand exposures of the monochromatic spectrum of G3 at $\lambda = 543.5$ nm. The level of the grass is more than 10^{-4} down from the strongest diffraction peak. The Lyman ghosts between the diffraction orders are less than 0.1% of the peak and are likely attributable to the photolithographic mask.

In gratings with poor surface quality, the amount of scattered light is large, and one observes a halo around the center of the spectrum. For good quality gratings, the large angular scale of the diffuse scattered light makes it very difficult to measure directly. Instead, we use atomic force microscopy (AFM) to directly measure the surface roughness ($\varepsilon_{\text{roughness}}$). For one of our grisms (G2) [2], we measured average $\varepsilon_{\text{roughness}}$ of 1.7 nm over a 2 μm × 2 μm area of groove surface. Height constraints in the AFM prevent us from measuring any of the immersion echelles discussed here, but we believe that the roughness of their grating surfaces should be comparable to the above figure. There is a wealth of information published about the temporal evolution of roughness of etched {100} surfaces [60,61], but little is available about {111} surfaces. Reference [62] discusses the roughness of {111} surfaces but only for aqueous KOH solutions without the addition of isopropanol and ultrasonic energy, both of which are known to improve the surface finish of etched {100} surfaces [52].

The total integrated light scattering is given approximately by [63]

$$\frac{I_{\text{diffuse}}}{I_0} = \left(\frac{2\pi n}{\lambda} 2\varepsilon_{\text{roughness}}\right)^2, \qquad (12)$$

where $\varepsilon_{\text{roughness}}$ is the rms surface roughness (e.g., as measured by the AFM). The summary of predicted I_{diffuse} for the grism device (G2) using Eq. (12) for several wavelengths and assuming $\varepsilon_{\text{roughness}} = 1.7$ nm is given in Table 5.

Surface microroughness may result from imperfections in silicon crystal (e.g., when the etch encounters an oxygen atom), H_2 bubbles that linger on the surface and block further reactions, or impurities in the KOH solution [64]. We have used both ultrasonic agitation and isopropanol to promote the H_2 bubble detachment. The silicon material we use has very low oxygen content, although it is unclear how much impurities actually affect immersion grating manufacture [50]. There are other sources of diffuse scattered light such as large groove defects (breaks in grooves, pyramid formations attributable to impurities in the crystal) that we are unable to account for in the predicted value from the AFM roughness measurement. Using visible light microscopes and SEM we find that the areal fraction of such macrodefects is less than 0.1% in our best gratings.

3. *Ghosts and Satellites*

When the error in groove positions is periodic, it can produce secondary images or ghosts. Historically, secondary images found symmetrically on each side

Table 5. Estimate of Microroughness from the AFM Data and Calculated Total Diffuse Scattered Light at λ = 632.8, 1.523, and 3.5 μm

Grating	$\varepsilon_{\text{roughness}}$	I_{diffuse}/I_0 λ = 632.8 nm	I_{diffuse}/I_0 λ = 1.523 μm[a]	I_{diffuse}/I_0 λ = 3.5 μm[a]
G2	1.7 nm	0.1%	0.2%	0.04%

[a]Estimates are given for grating used in immersion at 1.523 and 3.5 μm. The corresponding internal wavelengths are 441 and 1023 nm.

of a diffraction order and close to it have been called Rowland ghosts. Another type of ghosts found in gratings as a result of short-term periodic errors is called Lyman ghosts. In earlier tests, we observed Rowland ghosts in G0 which clearly derive from errors in the ruled mask that was used to pattern the substrate [5,58]. The period and amplitude of the groove spacing error are $P = 780\ \mu m$ and $A = 13.5$ nm. For gratings G1 and G3, we acquired photolithographic masks, which do not suffer from stitching and periodic errors [65]. The use of the new masks eliminated the periodic error in the dispersion direction. Ghosts are still present in both gratings, however, but displaced from the dispersion direction by 30° and match very well the orientation of the periodic wavefront error in the optical interferogram of G1 (Fig. 12, middle) [64]. We decided to apply the analysis appropriate for Rowland ghosts and compare the results to the optical interferometry data to determine whether the periodic pattern is indeed the source of ghosts in these two gratings.

The relationship between the period of the spacing error and the distance of the Rowland ghost from the parent line in Littrow configuration is [66]

$$\Delta x_M = M \frac{\lambda f}{P \cos \delta} \quad (13)$$

where Δx_M is the distance between the parent line and the Mth order Rowland ghost, and P is the period of the spacing error, while the relationship between the ghost intensity and the parent line intensity for the first pair of Rowland ghosts is given by

$$\frac{I_{\text{ghost}}}{I_{\text{line}}} = \left[\frac{2\pi n}{\lambda} A \sin \delta\right]^2, \quad (14)$$

where A is the amplitude of the spacing error, and I_{ghost} and I_{line} are the intensities of the ghost pair and the parent line, respectively. We deduce from Eq. (13) that $P = 5.6$ mm for G1, and $P = 0.61$ mm for G3. In the optical interferograms, these distances will be shortened by $\cos \delta$ in the dispersion direction. The projected period in the wavefront space is 5.1 mm for G1, close to the measured 4.0 mm from the fringes seen in the interferogram (see Fig. 12, middle). The displacement of the ghosts from the dispersion direction and the size of the period indicate that the spacing error is not attributable to errors in the mask pattern but rather to problems during the contact printing of the mask lines onto the photoresist layer, which we also confirmed visually by observing interference fringes while contacting the mask with the photoresist coated disks.

From the ghost intensities and Eq. (14) we derive $A = 23$ nm for G1, and $A = 9.2$ nm for G3. From the interferogram of G1, we estimate $A = 28\ \text{nm}/(\sin \delta) = 31$ nm, in excellent agreement with the direct measurement. The integrated intensity in the ghosts is 8.2% and 0.5% of parent line intensities for G1 and G3, respectively, at 1.523 μm in immersion.

Depending on the application, the ghosts seen in our gratings may not represent a problem. Since they are displaced in the spatial direction as well as in the dispersion direction, we can define the extent of each order in a cross-dispersed spectrograph to exclude contributions from ghost features. Since the intensities scale as $1/\lambda^2$, their contribution will drop to 1.5% in the spectrum of G1 (integrated in a pair of ghosts) at ~3.5 μm.

Resulting from nonperiodic errors in groove positions over a significant portion of a grating, satellites are spurious lines found very close to diffraction orders. We did not observe any satellites down to 10^{-5} of the strongest diffraction peak.

4. Conclusion

We have produced gratings appropriate for use in high-resolution IR spectrographs (R from 20,000 to 100,000) as immersion devices from 1.1 to 5 μm. We have developed a method to reliably produce gratings with arbitrary blaze angles and with groove spacings from a few micrometers to a few hundred micrometers. We have thoroughly tested and evaluated these gratings as front-surface as well as immersion devices and found that the results were consistent. As a result, it will be possible in the future to make a reliable determination of grating quality before several lengthy and costly cutting, polishing, and coating steps are carried out. The measured relative efficiencies of the immersion gratings are comparable to, or better than, those of the best commercially available front-surface echelle gratings but can operate in significantly higher orders. The one remaining area where there is substantial room for improvement is in reducing the level of repetitive errors introduced by our photolithographic patterning process. These errors do not affect performance for many applications. Nonetheless, we have devised several approaches to greatly reduce or eliminate them in our next batch of gratings.

This work was supported by NASA grants NAG5-9230 and NNG06GC45G, and by funding from McDonald Observatory at the University of Texas at Austin. J. P. Marsh acknowledges receipt of a NASA Graduate Research Program Fellowship (NGT5-137). The fabrication and testing of grating devices were made possible by facilities at the University of Texas at Austin, including the Center for Nano and Molecular Science and Technology (CNM), funded in part by the Welch Foundation, and the Microelectronics Research Center (MRC), funded in part by the NSF through the National Nanotechnology Infrastructure Network (NNIN). We thank R. Joyce, K. Hinkle, and G. Poczulp of the National Optical Astronomy Observatory for interferometer measurements. We thank K. Allers, S. Joshi, and J. Zhou for assistance in process development, and T. Gaubert and W. Frey for help with the AFM measurements. We also acknowledge helpful discussions with K. Ennico, A. Tokunaga, and P. Kuzmenko. Finally, we thank the referees for their constructive comments and suggestions.

References

1. O. A. Ershov, J. P. Marsh, K. N. Allers, and D. T. Jaffe, "Infrared grisms using anisotropic etching of silicon to produce a highly asymmetric groove profile," in *IR Space Telescopes and Instruments,* J. C. Mather, ed., Proc. SPIE **4850,** 805–812 (2003).
2. D. J. Mar, J. P. Marsh, D. T. Jaffe, L. D. Keller, and K. A. Ennico, "Performance of large chemically etched silicon grisms for infrared spectroscopy," in *Ground-Based and Airborne Instrumentation for Astronomy,* I. S. McLean and M. Iye, eds., Proc. SPIE **6269,** 62695R (2006).
3. U. U. Graf, D. T. Jaffe, E. J. Kim, J. H. Lacy, H. Ling, J. T. Moore, and G. Rebeiz, "Fabrication and evaluation of an etched infrared diffraction grating," Appl. Opt. **33,** 96–102 (1994).
4. D. T. Jaffe, L. D. Keller, and O. A. Ershov, "Micromachined silicon diffraction gratings for infrared spectroscopy," in *Infrared Astronomical Instrumentation,* A. M. Fowler, ed., Proc. SPIE **3354,** 201–212 (1998).
5. L. D. Keller, D. T. Jaffe, O. A. Ershov, T. Benedict, and U. U. Graf, "Fabrication and testing of chemically micromachined silicon echelle gratings," Appl. Opt. **39,** 1094–1105 (2000).
6. J. P. Marsh, D. J. Mar, and D. T. Jaffe, "Fabrication and performance of silicon immersion gratings for infrared spectroscopy," in *Ground-Based and Airborne Instrumentation for Astronomy,* I. S. McLean and M. Iye, eds., Proc. SPIE **6269,** 62694J (2006).
7. S. S. Vogt, S. L. Allen, B. C. Bigelow, L. Bresee, W. E. Brown, T. Cantrall, A. Conrad, M. Couture, C. Delaney, H. W. Epps, D. Hilyard, D. F. Hilyard, E. Horn, N. Jern, D. Kanto, M. J. Keane, R. I. Kibrick, J. W. Lewis, J. Osborne, G. H. Pardeilhan, T. Pfister, T. Ricketts, L. B. Robinson, R. J. Stover, D. Tucker, J. M. Ward, and M. Wei, "HIRES: the high-resolution echelle spectrometer on the Keck 10-m telescope," in *Instrumentation in Astronomy VIII,* D. L. Crawford and E. R. Craine, eds., Proc. SPIE **2198,** 362–375 (1994).
8. H. Dekker, S. D'Odorico, A. Kaufer, B. Delabre, and H. Kotzlowski, "Design, construction, and performance of UVES, the echelle spectrograph for the UT2 Kueyen telescope at the ESO Paranal Observatory," in *Optical and IR Telescope Instrumentation and Detectors,* M. Iye and A. F. M. Moorwood, eds., Proc. SPIE **4008,** 534–545 (2000).
9. R. Bernstein, S. A. Shectman, S. M. Gunnels, S. Mochnacki, and A. E. Athey, "MIKE: a double echelle spectrograph for the Magellan telescopes at Las Campanas Observatory," in *Instrument Design and Performance for Optical/Infrared Ground-Based Telescopes,* M. Iye and A. F. M. Moorwood, eds., Proc. SPIE **4841,** 1694–1704 (2003).
10. H.-U. Kaeufl, P. Ballester, P. Biereichel, B. Delabre, R. Donaldson, R. Dorn, E. Fedrigo, G. Finger, G. Fischer, F. Franza, D. Gojak, G. Huster, Y. Jung, J.-L. Lizon, L. Mehrgan, M. Meyer, A. Moorwood, J.-F. Pirard, J. Paufique, E. Pozna, R. Siebenmorgen, A. Silber, J. Stegmeier, and S. Wegerer, "CRIRES: a high-resolution infrared spectrograph for ESO's VLT," in *Ground-Based Instrumentation for Astronomy,* A. F. M. Moorwood and M. Iye, eds., Proc. SPIE **5492,** 1218–1227 (2004).
11. J. H. Lacy, M. J. Richter, T. K. Greathouse, D. T. Jaffe, Q. Zhu, and C. Knez, "TEXES: sensitive and versatile spectrograph for mid-infrared astronomy," in *Instrument Design and Performance for Optical/Infrared Ground-Based Telescopes,* M. Iye and F. M. Moorwood, eds., Proc. SPIE **4841,** 1572–1580 (2003).
12. M. Goto, K. Motohara, M. Imanishi, K. Sugiyama, K. Tomita, F. Iwamuro, and T. Maihara, "Development of a machine-cut metal grating for near-infrared spectroscopy," Publ. Astron. Soc. Pac. **110,** 841–847 (1998).
13. J. von Fraunhofer, "Neue Modifikation des Lichtes durch gegenseitige Einwirkung und Beugung der Strahlen, und Gesetze derselben," in *Denkschriften der königlichen Akademie der Wissenschaften zu München* **8,** 1821–1822 (1822), published in J. von Fraunhofer, *Gesammelte schriften. Im auftrage der mathematisch-physikalischen Classe der Königlich Bayerischen Akademie der München* (1888).
14. A. Leitner, "The life and work of Joseph Fraunhofer (1787–1826)," Am. J. Phys. **43,** 59–68 (1975).
15. E. Hulthén and H. Neuhaus, "Diffraction gratings in immersion," Nature **173,** 442–443 (1954).
16. L. Sica Jr., "High resolution diffraction grating," U.S. patent 4,475,792 (9 October 1984).
17. H. Dekker, "An immersion grating for an astronomical spectrograph," in *Instrumentation for Ground-Based Optical Astronomy, Present and Future,* L. B. Robinson, ed. (Springer-Verlag, 1988), p. 183.
18. C. G. Wynne, "Doubling spectral resolution," Mon. Not. R. Astron. Soc. **250,** 796–801 (1991).
19. R. Szumski and D. D. Walker, "The immersed echelle-I. Basic properties," Mon. Not. R. Astron. Soc. **302,** 139–144 (1999).
20. D. Lee and J. R. Allington-Smith, "An experimental investigation of immersed gratings," Mon. Not. R. Astron. Soc. **312,** 57–69 (2000).
21. G. Wiedemann and D. E. Jennings, "Immersion grating for infrared astronomy," Appl. Opt. **32,** 1176–1178 (1993).
22. P. J. Kuzmenko, D. R. Ciarlo, and C. G. Stevens, "Fabrication and testing of a silicon immersion grating for infrared spectroscopy," in *Optical Spectroscopic Techniques and Instrumentation for Atmospheric and Space Research,* J. Wang and P. B. Hays, eds., Proc. SPIE **2266,** 566–577 (1994).
23. H. U. Kaeufl, K. Kuehl, and S. Vogel, "Grisms from germanium/silicon for astronomical instruments," in *Infrared Astronomical Instrumentation,* A. M. Fowler, ed., Proc. SPIE **3354,** 151–158 (1998).
24. N. Ebizuka, M. Iye, and T. Sasaki, "Optically anisotropic crystalline grisms for astronomical spectrographs," Appl. Opt. **37,** 1236–1242 (1998).
25. F. Vitali, E. Cianci, D. Lorenzetti, V. Foglietti, A. Notargiacomo, E. Giovine, and E. Oliva, "Silicon grisms for high-resolution spectroscopy in the near-infrared," in *Optical and IR Telescope Instrumentation and Detectors,* M. Iye and A. F. Moorwood, eds., Proc. SPIE **4008,** 1383–1394 (2000).
26. N. Ebizuka, S.-Y. Morita, T. Shimizu, Y. Yamagata, H. Omori, M. Wakaki, H. Kobayashi, H. Tokoro, and Y. Hirahara, "Development of immersion grating for mid-infrared high dispersion spectrograph for the 8.2 m Subaru Telescope," in *Specialized Optical Developments in Astronomy,* E. Atad-Ettedgui and S. D'Odorico, eds., Proc. SPIE **4842,** 293–300 (2003).
27. J. Ge, D. McDavitt, B. Zhao, and S. Miller, "Large format silicon immersion gratings for high resolution infrared spectroscopy," in *Optomechanical Technologies for Astronomy,* E. Atad-Ettedgui, J. Antebi, and D. Lemke, eds., Proc. SPIE **6273,** 62732C (2006).
28. P. J. Kuzmenko, "Prospects for machined immersion gratings in the near-infrared and visible," in *Optomechanical Technologies for Astronomy,* E. Atad-Ettedgui, J. Antebi, and D. Lemke, eds., Proc. SPIE **6273,** 62733S (2006).
29. P. J. Kuzmenko, L. M. Little, P. J. Davis, and S. L. Little, "Modeling, fabrication, and testing of a diamond-machined germanium immersion grating," in *IR Space Telescopes and Instruments,* J. C. Mather, ed., Proc. SPIE **4850,** 1179–1190 (2003).
30. P. J. Kuzmenko, P. J. Davis, S. L. Little, L. M. Little, and J. V. Bixler, "High efficiency germanium immersion gratings," in *Optomechanical Technologies for Astronomy,* E. Atad-Ettedgui, J. Antebi, and D. Lemke, eds., Proc. SPIE **6273,** 62733T (2006).
31. J.-D. T. Smith, S. A. Rinehart, J. R. Houck, J. E. Van Cleve, J. C. Wilson, M. R. Colonno, J. Schoenwald, B. Pirger, and C. Blacken, "SCORE 1+: enhancing a unique mid-infrared spec-

trograph," in *Infrared Astronomical Instrumentation,* A. M. Fowler, ed., Proc. SPIE **3354,** 7980809 (1998).
32. Y. Ikeda, N. Kobayashi, S. Kondo, C. Yasui, K. Motohara, and A. Minami, "WINERED: a warm near-infrared high-resolution spectrograph," in *Ground-Based and Airborne Instrumentation for Astronomy,* I. S. McLean and M. Iye, eds., Proc. SPIE **6269,** 62693T (2006).
33. J. T. Rayner, "Evaluation of a solid KRS-5 grism for infrared astronomy," in *Infrared Astronomical Instrumentation,* A. M. Fowler, ed., Proc. SPIE **3354,** 289–294 (1998).
34. K. H. Hinkle, R. Drake, and T. A. Ellis, "Cryogenic single-crystal silicon optics," in *Instrumentation in Astronomy VIII,* D. L. Crawford and E. R. Craine, eds., Proc. SPIE **2198,** 516–524 (1994).
35. K. G. Lyon, G. L. Salinger, C. A. Swenson, and G. K. White, "Linear thermal expansion measurements on silicon from 6 to 340 K," J. Appl. Phys. **48,** 865–868 (1977).
36. Y. Okada and Y. Tokumaru, "Precise determination of lattice parameter and thermal expansion coefficient of silicon between 300 and 1500 K," J. Appl. Phys. **56,** 314–320 (1984).
37. C. J. Glassbrenner and G. A. Slack, "Thermal conductivity of silicon and germanium from 3 °K to the melting point," Phys. Rev. **134,** A1058–A1069 (1964).
38. H. Y. Fan and M. Becker, "Infrared absorption of silicon," Phys. Rev. **78,** 178–179 (1950).
39. W. Spitzer and H. Y. Fan, "Infrared absorption in n-type silicon," Phys. Rev. **108,** 268–271 (1957).
40. W. R. Runyan, *Silicon Semiconductor Technology* (McGraw-Hill, 1965).
41. G. G. MacFarlane, T. P. McLean, J. E. Quarrington, and V. Roberts, "Fine structure in the absorption-edge spectrum of Si," Phys. Rev. **111,** 1245–1254 (1958).
42. E. Bassous, "Fabrication of novel three-dimensional microstructures by the anisotropic etching of (100) and (110) silicon," IEEE Trans. Electron. Devices **25,** 1178–1185 (1978).
43. W. T. Tsang and S. Wang, "Preferentially etched diffraction gratings in silicon," J. Appl. Phys. **46,** 2163–2166 (1975).
44. E. Loewen, D. Maystre, E. Popov, and L. Tsonev, "Echelles: scalar, electromagnetic, and real-groove properties," Appl. Opt. **34,** 1707–1727 (1995).
45. J. Moore, H. Ling, U. U. Graf, and D. T. Jaffe, "A boundary integral approach to the scattering from periodic gratings," Microwave Opt. Technol. Lett. **5,** 480–483 (1992).
46. V. N. Mahajan, *Optical Imaging and Aberrations, Part II.* (SPIE Press, 2001).
47. B. Depuydt, P. M. Boone, P. Union, P. F. Muys, D. Vyncke, and C. Goessens, "Interferometric characterization of stress birefringence in germanium," in *Optical Inspection and Micromeasurements II,* C. Gorecki, ed., Proc. SPIE **3098,** 559–565 (1997).
48. D. L. Kendall, "On etching very narrow grooves in silicon," Appl. Phys. Lett. **26,** 195–198 (1975).
49. D. L. Kendall and R. Shoultz, "Wet chemical etching of silicon and 10 challenges for micromachiners," in *SPIE Handbook of Microfabrication, Micromachining, and Microlithography,* P. Rai-Choudhury, ed. (SPIE Optical Press, 1997), Vol. 2, pp. 41–97.
50. P. J. Kuzmenko and D. R. Ciarlo, "Improving the optical performance of etched silicon gratings," in *Infrared Astronomical Instrumentation,* A. M. Fowler, ed., Proc. SPIE **3354,** 357–367 (1998).
51. M. Madou, *Fundamentals of Microfabrication* (CRC Press, 1997).
52. T. Baum and D. J. Schiffrin, "AFM study of surface finish improvements by ultrasound in the anisotropic etching of Si⟨100⟩ in KOH for micromachining applications," J. Micromech. Microeng. **7,** 338–342 (1997).
53. H. Seidel, "The mechanism of anisotropic, electrochemical silicon etching in alkaline solutions," in *Solid-State Sensor and Actuator Workshop, 1990, 4th Technical Digest* (IEEE Press, 1990), pp. 86–91.
54. W. Van Gelder and V. E. Hauser, "The etching of silicon nitride in phosphoric acid with silicon dioxide as a mask," J. Electrochem. Soc. **114,** 869–872 (1967).
55. M. Born and E. Wolf, *Principles of Optics* (Cambridge U. Press, 1997).
56. D. J. Schroeder and R. L. Hilliard, "Echelle efficiencies: theory and experiment," Appl. Opt. **19,** 2833–2841 (1980).
57. E. W. Palmer, M. C. Hutley, A. Franks, J. F. Verrill, and B. Gale, "Diffraction gratings," Rep. Prog. Phys. **38,** 975–1048 (1975).
58. J. P. Marsh, O. A. Ershov, and D. T. Jaffe, "Silicon grisms and immersion gratings produced by anisotropic etching: testing and analysis," in *IR Space Telescopes and Instruments,* J. C. Mather, ed., Proc. SPIE **4850,** 797–804 (2003).
59. R. G. Tull, P. J. MacQueen, C. Sneden, and D. L. Lambert, "The high-resolution cross-dispersed echelle white-pupil spectrometer of the McDonald Observatory 2.7-m telescope," Publ. Astron. Soc. Pac. **107,** 251–264 (1995).
60. E. D. Palik, O. J. Glembocki, I. Heard, Jr., P. S. Burno, and L. Tenerz, "Etching roughness for (100) silicon surfaces in aqueous KOH," J. Appl. Phys. **70,** 3291–3300 (1991).
61. G. Findler, J. Muchow, M. Koch, and H. Münzel, "Temporal evolution of silicon surface roughness during anisotropic etching processes," in *Micro-Electro Mechanical Systems* (IEEE Press, 1992), pp. 62–66.
62. K. Sato, M. Shikida, T. Yamashiro, M. Tsunekawa, and S. Ito, "Roughening of single-crystal silicon surface etched by KOH water solution," Sens. Actuators A **73,** 122–130 (1999).
63. J. M. Bennett and L. Mattsson, *Introduction to Surface Roughness and Scattering,* 2nd ed. (Optical Society of America, 1999).
64. J. P. Marsh, "Production and evaluation of silicon diffractive optics for infrared astronomy," Ph.D. dissertation (The University of Texas at Austin, 2006).
65. B. J. Grenon, D. C. Defibaugh, D. M. Sprout, and C. J. Taft, "Manufacturing performance of the ALTA 3000 mask writer," in *Fifteenth Annual BACUS Symposium on Photomask Technology and Management,* G. V. Shelden and J. N. Wiley, eds., Proc. SPIE **2621,** 14–18 (1995).
66. G. W. Stroke, "Diffraction gratings," in *Handbuch der Physik* (Springer-Verlag, 1967), Vol. 29, pp. 426–758.